



Swansea University
Prifysgol Abertawe



Cronfa - Swansea University Open Access Repository

This is an author produced version of a paper published in :
The Journal of Physical Chemistry C

Cronfa URL for this paper:

<http://cronfa.swan.ac.uk/Record/cronfa34264>

Paper:

Wheeler, S., Bryant, D., Troughton, J., Kirchartz, T., Watson, T., Nelson, J. & Durrant, J. (2017). Transient Optoelectronic Analysis of the Impact of Material Energetics and Recombination Kinetics upon the Open-Circuit Voltage of Hybrid Perovskite Solar Cells. *The Journal of Physical Chemistry C*
<http://dx.doi.org/10.1021/acs.jpcc.7b02411>

This article is brought to you by Swansea University. Any person downloading material is agreeing to abide by the terms of the repository licence. Authors are personally responsible for adhering to publisher restrictions or conditions. When uploading content they are required to comply with their publisher agreement and the SHERPA RoMEO database to judge whether or not it is copyright safe to add this version of the paper to this repository.

<http://www.swansea.ac.uk/iss/researchsupport/cronfa-support/>

1 Transient Optoelectronic Analysis of the Impact of Material 2 Energetics and Recombination Kinetics on the Open-Circuit Voltage 3 of Hybrid Perovskite Solar Cells

4 Scot Wheeler,^{†,‡,§} Daniel Bryant,[†] Joel Troughton,[§] Thomas Kirchartz,^{||,⊥} Trystan Watson,[§]
5 Jenny Nelson,[‡] and James R. Durrant^{*,†,§,||}

6 [†]Department of Chemistry and [‡]Department of Physics, Imperial College London, South Kensington Campus, London SW7 2AZ,
7 United Kingdom

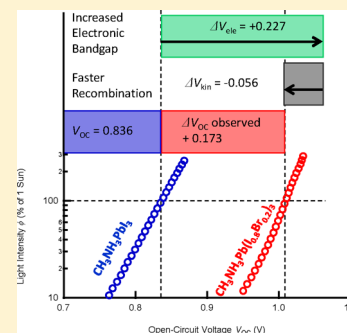
8 [§]SPECIFIC, College of Engineering, Swansea University, Swansea SA1 8EN, United Kingdom

9 ^{||}IEK5-Photovoltaics, Forschungszentrum Jülich, 52425 Jülich, Germany

10 [⊥]Faculty of Engineering and CENIDE, University of Duisburg-Essen, Carl-Benz-Strasse 199, 47057 Duisburg, Germany

11 **S** Supporting Information

12 **ABSTRACT:** Transient optoelectronic measurements were used to evaluate the factors
13 determining the open-circuit voltage of a series of planar photovoltaic devices based on
14 hybrid perovskite layers with varying iodine/bromine ratios. Employing differential charging
15 and transient photovoltage measurements, we used a simple device model based on the
16 charge-carrier-density dependence of nongeminate recombination to re-create correctly not
17 only the measured device open-circuit voltage (V_{OC}) as a function of light intensity but also
18 its dependence on bromine substitution. The 173 (± 7) mV increase in device voltage
19 observed with 20% bromine substitution is shown to result from a 227 (± 8) mV increase in
20 effective electronic band gap, which was offset in part by a 56 (± 5) mV voltage loss due to
21 faster carrier recombination. The faster recombination following 20% bromine substitution
22 can be avoided by indene- C_{60} bisadduct (ICBA) substitution into the [6,6]-phenyl- C_{61} -
23 butyric acid methyl ester (PCBM) electron-collection layer, resulting in a further 73 (± 7)
24 mV increase in device V_{OC} . These results are consistent with surface recombination losses at the perovskite/fullerene interface
25 being the primary limitation on the V_{OC} output of bromine-substituted devices. This study thus presents, and experimentally
26 validates, a simple model for the device physics underlying voltage generation in such perovskite-based solar cells and
27 demonstrates that this approach can provide key insights into factors limiting this voltage output as a function of material
28 energetics.



1. INTRODUCTION

29 Organic–inorganic lead halide perovskites are attracting
30 extensive interest for photovoltaic device applications. Rapid
31 progress has been made in device efficiencies, with several
32 recent studies reporting solar power conversion efficiencies
33 exceeding 20% for devices based on the ABX_3 perovskite
34 structure,^{1,2} with methylammonium lead halide (MAPX) being
35 the most well-known.^{3,4} Such promising device efficiencies are
36 motivating studies of the materials and device physics
37 underlying device function. One important performance
38 parameter determining photovoltaic device efficiency is the
39 open-circuit voltage, V_{OC} . Indeed, the remarkably high V_{OC}
40 values achieved for MAPX-based devices, approaching to within
41 0.4 V of the MAPX optical band gap, are a key factor behind
42 their high device efficiencies.^{5–7} However, at present, there is
43 no consensus on how photovoltage generation in perovskite
44 devices depends on variations in material composition and
45 device architecture. Several studies have provided evidence that
46 the energetics of both the perovskite active layer^{8,9} and the
47 electrodes^{5,10} are the important factors determining V_{OC} . It has

also been reported that methylammonium lead iodide (MAPI) 48
materials can exhibit remarkably long charge-carrier lifetimes in 49
films (given their high carrier mobilities),^{11–14} although the 50
relevance of these long carrier lifetimes to achieving high device 51
voltages is not as well-established. Herein, we report a transient 52
optoelectronic analysis of a series of planar junction perovskite 53
solar cells. The approach assesses the impacts of both kinetics 54
and energetics on device voltage. Employing a simple device 55
model, we demonstrate that, by using these transient 56
measurements, it is possible to successfully rationalize not 57
only the absolute device open-circuit voltage V_{OC} but also its 58
variation with light intensity and perovskite-layer halide 59
substitution. 60

Charge extraction (CE), small-perturbation transient photo- 61
current (TPC), and small-perturbation transient photovoltage 62
(TPV) have been shown to be powerful in situ probes of 63

Received: March 14, 2017

Revised: May 10, 2017

Published: June 6, 2017

charge-carrier accumulation and recombination and have been employed to demonstrate how changes in material energetics and charge-carrier recombination dynamics impact cell voltage in both organic and dye-sensitized solar cells.^{15–17} Although such transient optoelectronic measurements have previously been used to probe perovskite solar cells,^{18–22} the validity of this approach to understanding and reconstructing perovskite solar cell performance is yet to be demonstrated, due in part to the presence of hysteresis phenomena in the devices studied to date, which complicates both data measurement and analysis.²³ The planar hybrid organic–inorganic perovskite device structure utilizing the common organic interlayers poly(3,4-ethylenedioxythiophene):poly(styrene sulfonate) (PEDOT:PSS) and [6,6]-phenyl-C₆₁-butyric acid methyl ester (PCBM) is of interest to many because of the potential for low-cost, low-temperature solution processability with the added benefit of significantly reduced hysteresis.^{24–26} This reduced hysteresis, combined with a respectable photovoltaic performance and stability, makes these planar perovskite solar cells an ideal foundation for a detailed optoelectronic analysis of the materials and device physics underlying photovoltage generation in perovskite solar cells.

As an example system, we investigate the effect of exchanging iodide bromide in planar devices made from the CH₃NH₃Pb(I_{1-x}Br_x)₃ (MAPX) perovskite system. Bromide addition results in an increase in material band gap within a limited Br range and has been shown to lead to higher V_{OC} values.^{7–9,27–30} CH₃NH₃Pb(I_{1-x}Br_x)₃ therefore represents an example of a material series where the voltage appears to be determined, at least in part, by the perovskite energetics. We also investigate the effect of partially substituting PCBM with indene–C₆₀ bisadduct (ICBA) in the electron-collection layer to raise the energetics of this layer and, thereby, to investigate the role of Fermi-level pinning in such bromine-substituted devices. The first aim of this work was to investigate whether the transient optoelectronic techniques discussed above can be used to recreate correctly the open-circuit voltage of a planar MAPI solar cell and its dependence on light intensity, thereby testing a simple kinetic model of V_{OC}. Our second aim was to investigate whether this approach is able to quantify the contributions from materials energetics and from charge recombination dynamics to the observed variation in device V_{OC} with bromine and ICBA substitution.

2. EXPERIMENTAL SECTION

2.1. Fabrication. Cells were fabricated using a previously reported procedure.³¹ Indium tin oxide- (ITO-) coated glass substrates were coated with a PEDOT:PSS layer (P VP AL 4083, Heraeus) at 3500 rpm for 45 s and then subjected to annealing at 150 °C for 10 min. A perovskite precursor solution was made by dissolving a stoichiometric ratio of 1.25 M PbI₂ and methylammonium iodide in a mixture of dimethyl sulfoxide (DMSO) and γ -butyrolactone (GBL) (7:3) and stirring for 10 min. In the case when bromine was added, the ratios of PbBr₂ to methylammonium bromide and of PbI₂ to methylammonium iodide in the precursor solutions were adjusted to 0.9:0.1 and 0.8:0.2, respectively. Perovskite precursor solution was coated in a nitrogen-environment glovebox by a spin-coating procedure using two speeds, with toluene being dripped onto the surface during the second step. This was followed by drying at 100 °C post-deposition for 10 min. A [6,6]-phenyl-C₆₁-butyric acid methyl ester (PC₆₁BM) (Solenne) layer was deposited by spin coating of an 18 mg/mL solution in

chlorobenzene at 1000 rpm for 1 min. For ICBA:PCBM layers, a solution of indene–C₆₀ bisadduct (IC₆₁BA) (Solenne) was made by dissolving the solid in chlorobenzene at a concentration of 18 mg/mL. This solution was then added to the PC₆₁BM solution at a ratio of 20:80, after which the mixture was deposited by spin coating at 1000 rpm for 1 min. The cells were contacted by sequentially evaporating a Ca layer (5 nm) and an Al layer (150 nm), leaving an active area of 0.045 cm². The devices were then encapsulated using a glass coverslip and a UV-curable epoxy sealant (Ossila) for further testing.

2.2. J–V/EQE Measurements. Current density–voltage (J–V) characteristics were measured using a xenon lamp at AM1.5 solar illumination (Oriel Instruments) calibrated to a KG5 silicon reference cell with a Keithley 2400 source meter at a scan speed of 0.125 V/s.

External quantum efficiency (EQE) measurements were performed using a PV Measurements QEX10 system. Spectral response was measured between 300 and 850 nm in dc mode with a step size of 10 nm and calibrated using a silicon reference photodiode.

2.3. Transient Measurements. Transient photocurrent (TPC) and transient photovoltage (TPV) measurements and analysis were carried out as previously reported.³² To briefly summarize, background illumination was provided by a ring of 12 white light-emitting diodes (LEDs) capable of a power of up to 4 sun equivalents, calibrated to the short-circuit current density (J_{SC}) as measured under simulated AM1.5 illumination. Any changes in background illumination or bias conditions were followed by a wait time greater than 2 s before measurements commenced to avoid effects of hysteresis as a result of these conditions. Although still expected, the hysteresis equilibrates considerably faster than for the architecture investigated.²⁴ During TPV measurements, the device was held at a range of open-circuit conditions utilizing the 1 M Ω input impedance of a Tektronix TDS3032 oscilloscope and controlled by the background illumination. Following a small optical excitation provided by a pulsed Continuum Minilite Nd:YAG laser at 532 nm with a pulse width of <10 ns, the resulting small-perturbation voltage transient decay, measured on the oscilloscope, was fitted with a monoexponential to obtain the small-perturbation carrier lifetime. The intensity of the small optical excitation, which remained constant under all background illumination conditions, was set to achieve a voltage perturbation of less than 20 mV at 1-sun background illumination to operate within the small-perturbation regime; however, the perturbation also had to be large enough to be distinguished at higher light intensities (as the voltage deflection decreased at higher density of state population). During TPC measurements, the device was held close to short-circuit conditions with a 50 Ω measurement resistance. The resulting current transient from the same excitation as for TPV measurements was integrated to obtain an estimate of the number of carriers generated by the laser excitation. A value for the total charge Q at low background light intensity (<20% sun) was used for differential charging analysis to avoid nonlinear recombination losses at short circuit that could be present at high light intensities. Key assumptions of TPC/TPV measurements require the extra charge to equilibrate with the device electrodes prior to recombination and generation to be independent of applied field between short circuit and open circuit in high-permittivity materials. Fitting of the experimental data was typically done at light intensities greater than 10% of 1-sun equivalent background illumination; this should be within

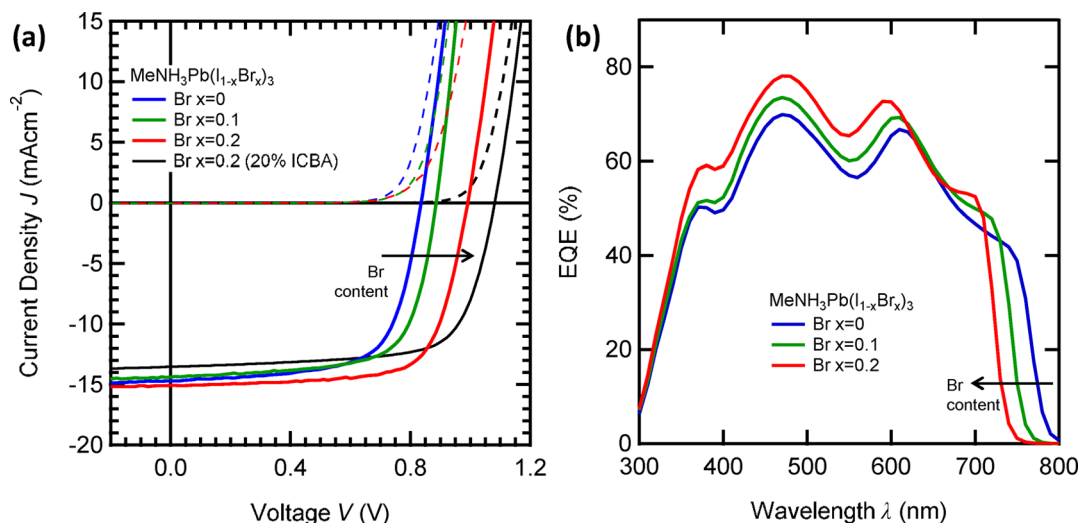


Figure 1. Device performance: (a) AM1.5 J - V response and (b) EQE of ITO/PEDOT:PSS/CH₃NH₃(I_{1-x}Br_x)₃/PC₆₀BM/Ca/Al as a function of bromine composition. The increase in perovskite band gap with increasing Br content led to an increase in the device V_{OC} value. The black J - V curve corresponds to an $x = 0.2$ device with 20% ICBA added to the PCBM, which increased the V_{OC} value further.

Table 1. Comparison of Energy Shifts Relative to CH₃NH₃PbI₃ as a Function of Br Content in CH₃NH₃Pb(I_{1-x}Br_x)₃ Planar Cells

Br content	ΔV_{OC}^a (± 0.007) (V)	ΔE_{opt}^b (± 0.09) (eV)	ΔV_{ele}^c (± 0.009) (V)	ΔV_{kin}^d (± 0.005) (V)	ΔV_{eff} ($\Delta V_{ele} + \Delta V_{kin}$) (± 0.010) (V)
0 \rightarrow 0.10	+0.026	+0.07	+0.081	-0.053	+0.028
0 \rightarrow 0.20	+0.173	+0.12	+0.227	-0.056	+0.171

^a V_{OC} from J - V curves at 1 sun. ^b ΔE_{opt} from optical absorption measurements (Figure S1). ^cEffective electronic band-gap shift (ΔV_{ele}) from n vs V_{OC} (Figure 3a) at $3.5 \times 10^{15} \text{ cm}^{-3}$. ^dKinetic shift (ΔV_{kin}) from τ vs n (Figure 3b) at $3.5 \times 10^{15} \text{ cm}^{-3}$.

188 the small-perturbation regime and avoids the V_{OC} shunt-limited
189 regime at low light intensity.

3. RESULTS

190 **3.1. Device Characterization.** Figure 1 shows plots of the
191 J - V performance and external quantum efficiency (EQE)
192 spectra of the planar hybrid perovskite solar cells studied in this
193 work. Devices were fabricated with the device structure ITO/
194 PEDOT:PSS/CH₃NH₃Pb(I_{1-x}Br_x)₃/PC₆₁BM/Ca/Al following
195 literature procedures, as detailed in the Experimental Section.
196 Perovskite and PC₆₀BM layer thicknesses were consistently
197 measured to be 300 and 30 nm (± 5 nm), respectively, for all
198 devices. We focus on the range of Br contents x from 0 to 0.2;
199 higher levels of bromide substitution resulted in large losses of
200 device performance and reproducibility, due to the disruption
201 of the crystal structure and probable light-induced halide
202 segregation. This light-induced halide segregation, which has
203 been well-documented in films, remains largely unstudied in
204 devices.^{9,33-36} Although not observed in the range of
205 compositions studied, we believe that the methods demon-
206 strated herein would be well-suited for further study of these
207 phenomena. Cells were measured under simulated AM1.5
208 illumination and exhibited negligible hysteresis over the scan
209 speeds and temperatures employed (see Figure S2 in the
210 Supporting Information). Box plots of the device-to-device
211 performance variability can also be found in the Supporting
212 Information (Figure S3). Devices employed for the transient
213 studies reported herein showed device efficiencies ranging from
214 8.3% ($\pm 0.2\%$) for the CH₃NH₃PbI₃ device to 10.7% ($\pm 0.2\%$)
215 for the CH₃NH₃Pb(I_{0.8}Br_{0.2})₃ device, slightly lower than the
216 initial device performance following fabrication (as reported in
217 Figure S3) due to initial degradation or burn-in. This decrease

is primarily associated with lower current density, with V_{OC} 218
remaining largely stable; further degradation over the course of 219
the measurements was not observed. Although the device 220
performance reported is lower than the top efficiencies 221
reported for this architecture, the associated trends, particularly 222
in V_{OC} , as is the focus herein, with the range of Br contents 223
studied are consistent with the results of Noh et al. and other 224
higher-performing examples.^{8,9,27} All devices showed good 225
linearity of J_{SC} as a function of light intensity (Figure S4), 226
suggesting that nonlinear recombination processes are not a 227
significant limitation at short circuit because of good charge 228
collection. This study focused instead on the impact of 229
recombination losses on V_{OC} . It is apparent that substitution 230
of 20% bromide into the material resulted in an increase in V_{OC} 231
from 0.836 (± 0.005) V to 1.009 (± 0.005) V (Figure 1a), 232
correlated with an increase in the optical band gap from 1.56 233
(± 0.09) eV (795 nm) to 1.68 (± 0.09) eV (738 nm) 234
(determined from the optical absorbance onset), as is apparent 235
from the EQE spectrum (Figure 1b) and the optical absorbance 236
spectrum (Figure S1). It is of particular note that the change in 237
 V_{OC} (173 mV) was almost 50% larger than the change in 238
optical band gap (120 meV), as detailed in Table 1, clearly 239
indicating that measurements of the optical band gap alone are 240
not a quantitative indicator of changes in cell voltage. A further 241
73 (± 7) mV increase in voltage was observed for 20% bromide 242
with the substitution of 20% ICBA into the PCBM electron 243
layer, as discussed further below. In this study, we combined 244
differential charging as a measure of electronic, rather than 245
optical, band gap with transient photovoltage measurements of 246
carrier lifetime to obtain a quantitative understanding of device 247
 V_{OC} . 248

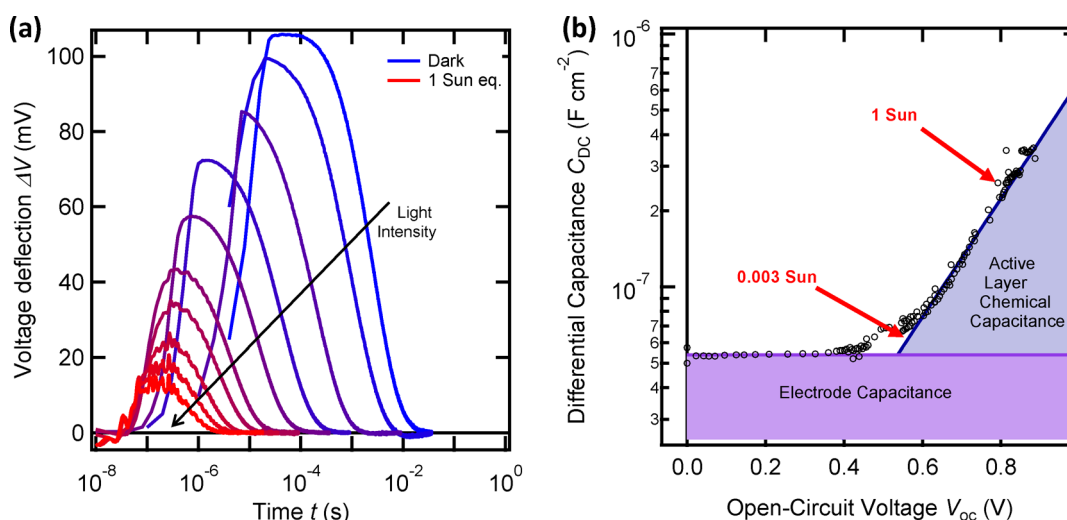


Figure 2. Transient voltage and capacitance response: (a) Decay of the transient photovoltage over a range of light intensities between darkness and 1 sun for a pure MAPI planar hybrid perovskite. (b) Differential capacitance measured from transient photocurrent and transient photovoltage as a function of the open-circuit voltage (V_{OC}) over a range of background light intensities from 0 to 5 sun equivalents.

249 **3.2. Optoelectronic Measurements.** The kinetic ap-
 250 proach applied herein to analyze V_{OC} is based on the balance
 251 between carrier generation, $J_{gen}(V)$, and recombination
 252 currents, $J_{loss}(V)$. At V_{OC} under steady-state conditions, no
 253 external current flows; therefore, the generation and recombina-
 254 tion currents must be equal: $J_{gen}(V_{OC}) = J_{loss}(V_{OC})$. The size
 255 of V_{OC} can therefore be understood if both the generation
 256 current and the recombination current can be measured. We
 257 assumed carrier generation efficiency to be voltage-independent
 258 between short circuit and open circuit for high-permittivity
 259 perovskite materials. If recombination losses at short circuit are
 260 low because of sufficiently fast carrier extraction, as supported
 261 for the cells herein by observation of a linear dependence of J_{SC}
 262 on light intensity (Figure S4), we can use $J_{gen}(V) = J_{gen} = J_{SC}$ for
 263 each light intensity employed.

264 Small-perturbation transient photovoltage (TPV) decays
 265 were employed as an assay of charge-carrier recombination;
 266 typical transients are shown in Figure 2a for $\text{CH}_3\text{NH}_3\text{PbI}_3$
 267 device as a function of background light intensity. In all cases,
 268 the decays could be reasonably fitted by single-exponential
 269 decays (Figure S10), consistent with the small-perturbation
 270 limit employed in these studies. We note that this situation
 271 contrasts with previous TPV analyses of perovskite devices
 272 employing mesoporous titania electron-collection layers, which
 273 exhibited more complex biexponential decays, associated with
 274 the hysteresis phenomena observed in these devices.^{18,22} It is

275 also apparent that the time scale of the TPV decays observed
 276 for the $\text{CH}_3\text{NH}_3\text{PbI}_3$ device studied herein varies by several
 277 orders of magnitude with light intensity, with exponential decay
 278 times ranging from 1.60 ms at 9×10^{-5} sun equivalent
 279 (corresponding to $V_{OC} = 0.429$ V) to $0.59 \mu\text{s}$ at 1 sun
 280 (corresponding to $V_{OC} = 0.813$ V). This strong dependence is
 281 indicative of charge recombination in these devices accelerating
 282 strongly as the charge density in the device is increased under
 283 stronger irradiation. Such a dependence is at least qualitatively
 284 consistent with transient optical studies of excitation-intensity-
 285 dependent bimolecular recombination in $\text{CH}_3\text{NH}_3\text{PbI}_3$ films.³⁷

286 We now turn to an analysis of the charge density in the
 287 device at open-circuit voltage over a range of light intensities
 288 relevant for typical device operation. To perform this analysis,
 289 we use the method of differential charging (DC), a

combination of transient photocurrent (TPC) and transient
 290 photovoltage (TPV) measurements.^{15,18} The differential
 291 capacitance C_{DC} is calculated at each V_{OC} value as
 292

$$C_{DC} = \frac{\Delta Q}{\Delta V_0(V_{OC})} \quad (1) \quad 293$$

294 where ΔQ is the short-circuit photogenerated charge from the
 295 small-perturbation laser pulse, measured from the TPC, and
 296 ΔV_0 is the corresponding initial open-circuit voltage deflection
 297 during TPV. We note that charge extraction, a widely used
 298 alternative method for determining charge density, gave
 299 unreasonably large charge densities, as has been noted
 300 previously,¹⁸ and so was not used in this study (see the
 301 Supporting Information for a discussion of this point).
 302 Crucially, DC provides a small-perturbation measurement
 303 that does not involve a large switch in internal field during
 304 the measurements; rather, measurements at short circuit and
 305 open circuit are undertaken independently under steady-state
 306 conditions after any significant hysteresis or polarization.

307 The differential capacitance for a representative
 308 $\text{CH}_3\text{NH}_3\text{PbI}_3$ planar device can be seen in Figure 2b. It is
 309 apparent that this capacitance exhibits two regimes depending
 310 on the size of the quasi-Fermi-level splitting of V_{OC} (controlled
 311 by the background light intensity). At low light levels, the
 312 differential capacitance is independent of voltage and has a
 313 value of 55.5 nF cm^{-2} . This capacitance is in reasonable
 314 agreement with the geometric capacitance of the device
 315 electrodes, which is expected to dominate at low quasi-Fermi-
 316 level splitting, corresponding to an effective relative dielectric
 317 constant for MAPI of 19, consistent with values reported by
 318 others for this type of device.^{38,39} This capacitance is therefore
 319 assigned to charging of the device electrodes, with electrode
 320 charge constituting a significant fraction of charge accumulation
 321 at low light levels. At an equivalent light intensity of 0.3% of 1
 322 sun, there is a transition to the differential capacitance varying
 323 approximately exponentially with voltage, with a slope in the
 324 range of $(0.2-0.33)kT$. This can be primarily assigned to the
 325 chemical capacitance of the active layer, corresponding to the
 326 charge stored in the perovskite photoactive layer as the quasi-
 327 Fermi levels approach the semiconductor conduction- and

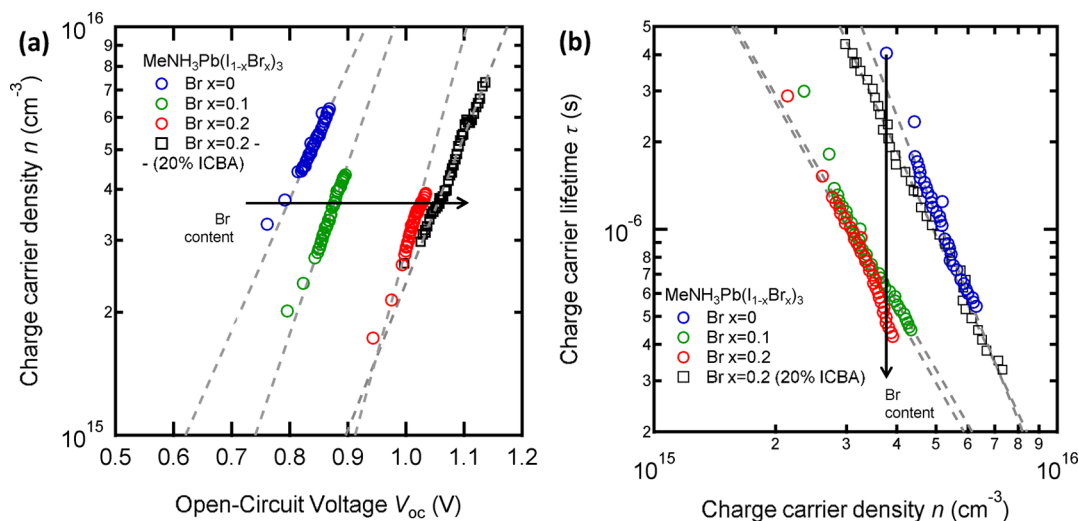


Figure 3. Optoelectronic characterization: (a) Active-layer charge-carrier density (n_{AL}) as a function of quasi-Fermi-level splitting (V_{OC}). (b) Average charge-carrier lifetime (τ) as a function of n_{AL} for $\text{CH}_3\text{NH}_3\text{Pb}(\text{I}_{1-x}\text{Br}_x)_3$ cells with Br contents of $x = 0, 0.1$, and 0.2 . The same approximate range of light intensities, between 0.1 and 3 sun equivalents, was used for each material system. The results for the use of 20% ICBA in PCBM for the $x = 0.2$ device is shown with black squares. Gray dashed lines represent fits according to (a) eq 2 and (b) eq 3.

328 valence-band edges, supported by our studies as a function of
329 bromide substitution, as discussed below.

330 The total excess charge Q stored in the device at open circuit
331 (V_{OC}) can be calculated by integration of the differential
332 capacitance with V_{OC} .¹⁵ Using this integration, we found the
333 total excess charge present in the device under 1-sun conditions
334 at open circuit to be 70 nC cm^{-2} (shown in Figure S8), with
335 approximately 45% stored in the perovskite layer (correspond-
336 ing to a charge density of $6.6 \times 10^{15} \text{ cm}^{-3}$) and the remainder
337 on the device electrodes.

338 We note that the decay dynamics of TPC transients used to
339 determine C_{DC} exhibited decay times similar to, and in some
340 cases slower than, the TPV transients at similar light intensities
341 (Figure S9), unusual for a material system known for high fill
342 factors (FFs) and efficient collection at short circuit. These
343 slower TPC decay dynamics appear to be RC-limited,
344 associated in particular with slow transport dynamics in the
345 PCBM electron-collection layer. The RC time constant for the
346 MAPI device studied above is $0.8 \mu\text{s}$, determined from the
347 electrode capacitance of 55.5 nF cm^{-2} measured above and the
348 measured device series resistance of 150Ω , in good agreement
349 with our measured TPC decay kinetics (see Figure S9). (This
350 RC limitation does not impede the validity of our differential
351 capacitance analysis, as discussed in the Supporting Informa-
352 tion.) The origin of this relatively slow RC time constant was
353 investigated by varying the PCBM layer thickness (see Figure
354 S6) and using the TPV rise time as a transport measurement
355 that avoids the RC limitations.⁴⁰ At low irradiance conditions,
356 where the electrode capacitance dominates over the active-layer
357 capacitance and, therefore, the generation of cell voltage
358 requires electron transport through the PCBM to the metal top
359 electrode, the photovoltage rise time was observed to increase
360 from being instrument-response-limited (190 ns) for a 40-nm
361 PCBM layer to 250 ns for a 150-nm -thick layer, correlated with
362 an increase in sheet resistance (R_s) from 55 to 150Ω . Using the
363 voltage drop across the low-dielectric PCBM ($V_{PCBM} = V_{bi}C_{tot}/$
364 C_{PCBM} , where V_{bi} is the built-in voltage, C_{tot} is the total
365 capacitance, and C_{PCBM} is the capacitance of PCBM), a drift
366 carrier mobility of $9.7 \times 10^{-4} \text{ cm}^2 \text{ V}^{-1} \text{ s}^{-1}$ can be estimated (see
367 Supporting Information), consistent with literature data,^{41,42}

and significantly lower than the high reported mobilities in
368 MAPI ($1 \text{ cm}^2 \text{ V}^{-1} \text{ s}^{-1}$).¹¹ As well, the J - V curve for the thick
369 PCBM layers (Figure S7) shows a reduced fill factor and the
370 presence of an S-shape, consistent with a buildup of space
371 charge due to the restriction of carriers out of the device.⁴³
372 Both results are indicative of the charge extraction from the
373 device (and therefore the cell resistance) being limited by the
374 PCBM layer.

3.3. Energetics and Recombination Kinetics. We now
375 turn to a consideration of the impact of bromide substitution
376 on the charge accumulation and recombination dynamics and,
377 thereby, on the cell voltage in the planar perovskite cells studied
378 herein. We focus on the high-light-level regime (10 – 300% of 1
379 sun) most relevant to practical device operation, where, for all
380 devices, the active-layer chemical capacitance was determined
381 to dominate over the electrode capacitance. Figure 3a shows
382 the total average excess charge density in the active layer, n_{AL} ,
383 at open circuit as calculated from differential charging for cells
384 with varying bromine contents. In comparison to the values for
385 typical organic photovoltaic (OPV) devices,^{32,44} n_{AL} was
386 observed to be lower for the perovskite devices studied herein,
387 consistent with the faster bimolecular recombination kinetics
388 limiting charge accumulation in the active layer of the
389 perovskite devices at open circuit. At low light levels, all
390 devices exhibited similar dependencies of the total accumulated
391 charge Q on V_{OC} , consistent with this charge being associated
392 with the electrode capacitance, independent of the active-layer
393 energetics (see Figure S12). At higher light levels, for all
394 devices, the charge started to increase exponentially with V_{OC} ,
395 assigned as above to increasing charge accumulation in the
396 active layer of the device. Bromide substitution was observed to
397 result in an increase in the voltage at which this active-layer
398 charge accumulation started to dominate over electrode charge.
399 This is consistent with the increase in perovskite band gap with
400 bromide substitution, as indicated by the optical measurements
401 above, and confirms our assignment of this exponentially
402 increasing charge to active-layer charge.

403 More quantitatively, n_{AL} was well fitted to the exponential
404 function
405

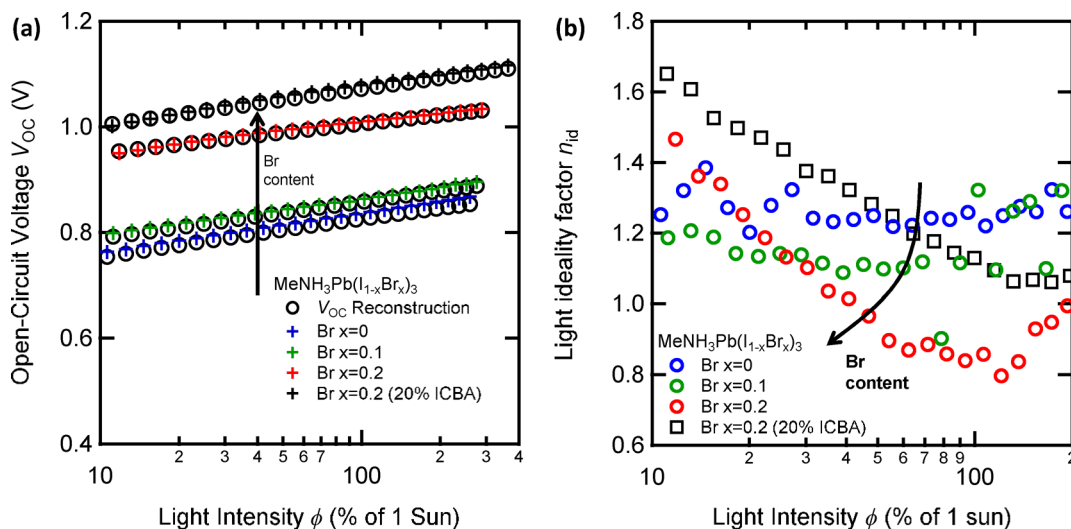


Figure 4. Light-intensity-dependent V_{OC} and ideality factor: (a) Measured (crosses) and reconstructed (circles) open-circuit voltage values as a function of illumination intensity for $\text{CH}_3\text{NH}_3\text{Pb}(\text{I}_{1-x}\text{Br}_x)_3$ cells with Br contents of $x = 0, 0.1,$ and $0.2.$ (b) Light ideality factor as a function of light intensity, calculated from the slope of V_{OC} versus light intensity. The effect of adding 20% ICBA to the PCBM is shown in black.

$$n_{AL} = n_0 \exp\left(\frac{qV_{OC}}{mk_B T}\right) \quad (2)$$

407

where n_0 and m are experimentally derived constants. m specifies how the slope of $n(V_{OC})$ deviates from the thermal voltage kT/q . Values of m for the cells studied here were in the range of 3–5, decreasing slightly with increasing bromide content. Although in certain situations m can be used as a measure of the shape of the density of states, it can be influenced by factors such as doping or surface recombination as a result of spatially inhomogeneous charge distributions.⁴⁵ If we assume the simple relation $n \propto \exp(qV/2E_{ch})$, where E_{ch} is the characteristic energy (see ref 45 for more details), to be valid for intrinsic semiconductors, slopes in the range $3 < m < 5$ suggest a characteristic energy for the density of states of 37.5–62.5 meV. The shift of n_{AL} with bromide substitution allows for the quantification of the increase in the effective electronic band gap with increasing bromide concentration. We note that the term “effective electronic band gap” refers to the onset of charge accumulation as a function of quasi-Fermi-level splitting; this might differ from the threshold for photon absorption characterized by the optical band gap due to the presence of optically dark states and polaronic or excitonic effects. Taking $3.5 \times 10^{15} \text{ cm}^{-3}$ as a representative charge density, we conclude that 10% bromide substitution results in an 81 ± 9 meV increase in this effective electronic band gap and 20% substitution results in a 227 ± 9 meV increase. We note that these increases in effective electronic band gap with bromine substitution are larger than the increases in optical band gap discussed above (see Table 1 for a comparison).

Before considering the impact of this increased effective electronic band gap on V_{OC} , we address the impact of bromide substitution on the charge-carrier lifetimes. TPV transients analogous to those shown in Figure 2a were collected as a function of bromide substitution. These TPV transients were fitted using a monoexponential from which the small-perturbation carrier lifetime $\tau_{\Delta n}$ was determined. $\tau_{\Delta n}$ can be related to the pseudo-first-order carrier lifetime $\tau_n = \delta\tau_{\Delta n}$, an average of all potential recombination mechanisms across the entire device, where δ is the overall recombination order with

respect to n as defined by $J_{loss} = kn^\delta$, where k is a rate coefficient independent of n . The dependence of carrier lifetime on carrier density is plotted in Figure 3b. It is apparent that the carrier lifetime exhibits a power-law dependence on charge density, as expected for a bimolecular charge recombination process of the form

$$\tau_n = \tau_{n_0} \left(\frac{n}{n_0}\right)^{(1-\delta)} \quad (3)$$

where n_0 was defined above and τ_{n_0} is an experimentally derived constant from the voltage dependence of τ_n . Further discussion and derivations can be found in the Supporting Information and elsewhere.^{17,32,44,46} This pseudo-first-order carrier lifetime for all three compositions is seen to have an approximate n^{-2} ($\delta \approx 3$) dependence on active-layer charge-carrier density, over the range of n values studied. Further interpretation of this order would be unwise without further knowledge of doping densities and the spatial distribution of charges; however, in an undoped and sufficiently thick device, it would be compatible with recombination through trap states.⁴⁶ We note that this bimolecular recombination will include both radiative and nonradiative recombination processes.

When comparing the recombination dynamics of material systems with different energetic profiles, it is important to address how lifetime varies with carrier density, rather than cell voltage. It is apparent from Figure 3b that, for matched carrier densities, the recombination lifetime was shortened by addition of Br to the perovskite structure. This acceleration of charge recombination losses with bromine substitution was also apparent from approximately 2-fold lower accumulated charge densities observed for the bromine-substituted devices for matched light intensities (see Figure 3a). Again, taking $3.5 \times 10^{15} \text{ cm}^{-3}$ as a representative charge density, one can see from Figure 3b a shortening of the lifetime from $4.08 (\pm 0.23) \mu\text{s}$ in $\text{CH}_3\text{NH}_3\text{PbI}_3$ to $0.80 (\pm 0.08) \mu\text{s}$ at 10% bromide content and $0.73 (\pm 0.04) \mu\text{s}$ at 20% bromide content, indicating a 5-fold reduction in carrier lifetime following bromine substitution, calculated to result in a $56 (\pm 5) \text{ mV}$ loss of cell voltage (see the Supporting Information for calculation details). This shortening

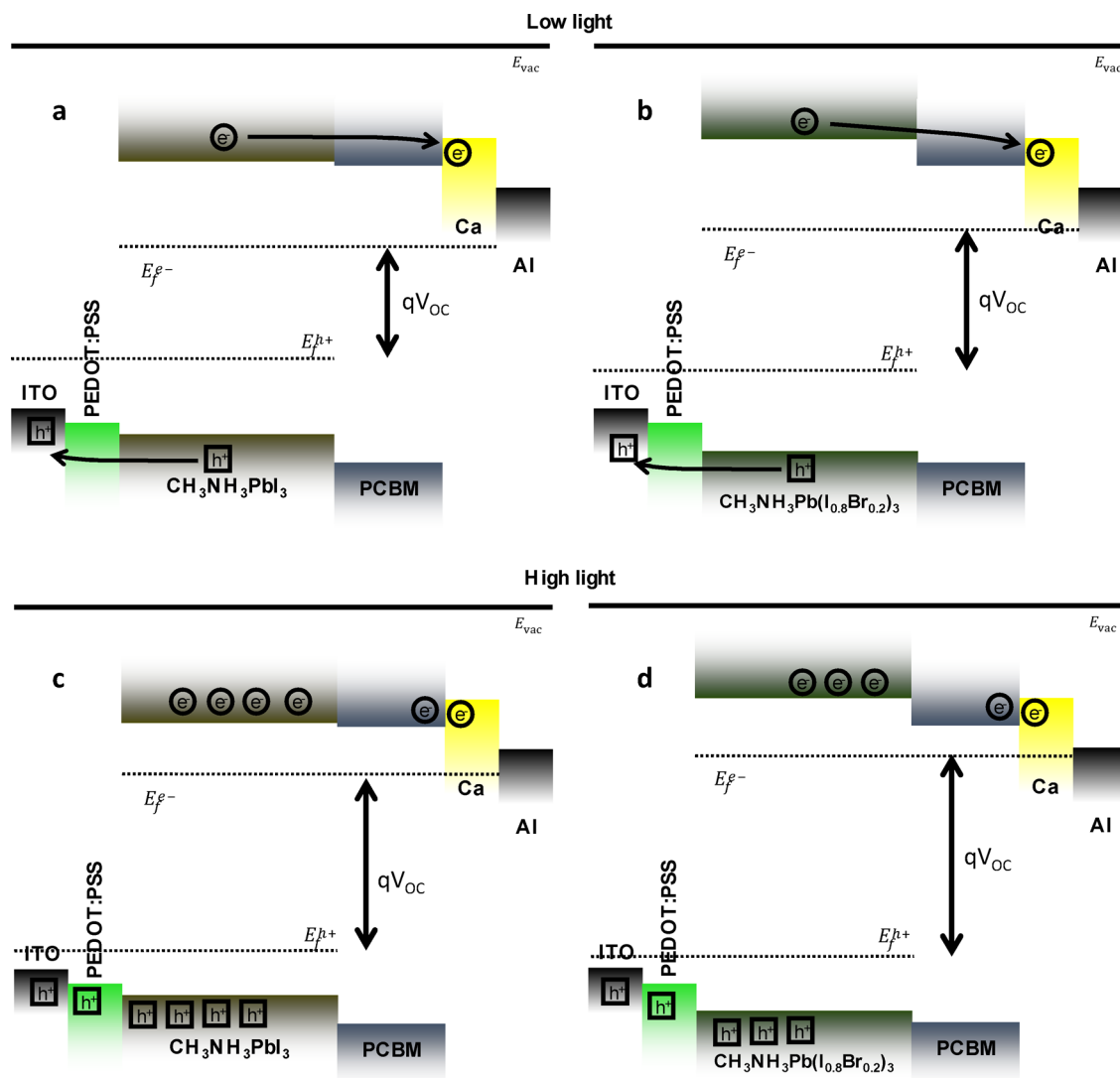


Figure 5. Energy diagrams: (a,c) $\text{CH}_3\text{NH}_3\text{PbI}_3$ and (b,d), $\text{CH}_3\text{NH}_3\text{Pb}(\text{I}_{0.8}\text{Br}_{0.2})_3$. (a,b) Low light intensity, where charges are mostly on the electrodes. (c,d) Light intensity closer to 1 sun, where charges begin to build up in the active layer. Even though panel d shows a greater voltage than panel c because of the increase in band gap, faster recombination leads to less charge in the active layer and quasi-Fermi levels that are not able to approach the band edges as much.

482 of carrier lifetime tends to decrease the photovoltage for a given
483 J_{gen} value, somewhat opposing the shift in the density of states
484 to higher energies with increasing Br content, as seen in Figure
485 3a.

486 **3.4. V_{OC} Reconstruction and Device Ideality.** If this
487 description of in situ energetics and recombination kinetics is
488 accurate, it should be possible to reconstruct the V_{OC} of the
489 measured devices over the range of light intensities studied. As
490 discussed above, at open circuit, the recombination loss current
491 $J_{\text{loss}} = (q \, dn)/\tau_n$ must be equal to the generation current J_{gen} ,
492 assumed to equal J_{SC} . From eqs 2 and 3, it is possible to obtain
493 a simple expression for V_{OC} as

$$V_{\text{OC}}^{\text{calc}} = \frac{mk_{\text{B}}T}{q\delta} \ln\left(\frac{J_{\text{SC}}\tau_{n_0}}{q \, dn_0}\right) \quad (4)$$

495 where all of the terms were obtained directly from our
496 measured TPV decays and DC data and J_{SC} was measured
497 under the same irradiation conditions at short circuit. Figure 4a
498 shows the resulting calculated device open-circuit voltages $V_{\text{OC}}^{\text{calc}}$
499 determined using eq 4 overlaid on the directly measured

voltages V_{OC} . It is apparent that there is excellent agreement 500
(± 5 mV) between our calculated and measured values for V_{OC} . 501
Thus, our simple device model and transient optoelectronic 502
analyses are able to yield not only the correct absolute open- 503
circuit voltage for these devices but also the variation of the 504
voltage with light intensity and bromine substitution. The 505
excellent correlation between the calculated and measured V_{OC} 506
values over such a range of light intensities, reflecting real-life 507
operating conditions, demonstrates the applicability of the 508
discussed optoelectronic techniques in the study of perovskite 509
photovoltaics. This agreement, along with the data in Table 1, 510
furthermore demonstrates how energetic changes and kinetic 511
changes combine to give the observed device voltage. 512

Finally, Figure 4b shows the light ideality factor, as calculated 513
from the derivative of the voltage as a function of light intensity, 514
 $n_{\text{id}} = (q \, dV_{\text{OC}})/\{kT[d \ln(\phi)]\}$.⁴⁷ A value of 1 is nominally 515
assigned to the recombination of free charges or to 516
recombination at the semiconductor electrode interfaces, 517
whereas a value of 2 is assigned to the recombination of free 518
charge with a trap state toward midgap.⁴⁸ The observed values 519

520 for n_{id} for the devices studied herein are in the range of 1–1.5,
521 that is, lower than the values of $n_{\text{id}} \approx 2$ commonly reported in
522 the literature.^{3,49,50} The open-circuit voltages obtained in our
523 devices are substantially lower than the radiative open-circuit
524 voltage of MAPI, which is about 1.33 V,^{51,52} indicating that
525 radiative free-carrier recombination, one possible source of $n_{\text{id}} =$
526 1, is not dominant in our devices. Figure 4b shows the n_{id}
527 decreased as the Br content was increased. In the case of 20%
528 Br, a clear reduction in n_{id} with increasing light intensity can be
529 seen. This is a common observation for devices in surface
530 recombination becomes a dominant loss pathway, resulting in
531 increased Fermi-level pinning as V_{OC} approaches the built-in
532 voltage V_{bi} .^{43,47}

533 To further investigate the potential for surface recombination
534 at the perovskite/fullerene interface to limit V_{OC} of the
535 bromine-substituted devices, devices with 20% Br content were
536 fabricated with the PCBM layer containing 20% ICBA. ICBA
537 has a higher-lying lowest unoccupied molecular orbital
538 (LUMO) energy than PCBM and, therefore, has the potential
539 to reduce the energy offset between the perovskite and
540 fullerene layers. An ICBA content of 20% was the best-
541 performing PCBM/ICBA ratio and was chosen to emphasize
542 the improvement in V_{OC} , and reduction in V_{OC} pinning, that
543 can be achieved through a simple modification of the interlayer.
544 The J – V performance in Figure 1a shows a further increase in
545 device V_{OC} of 73 (± 7) mV to 1.082 (± 0.005) V. The
546 corresponding energetic and kinetic data are shown in Figure 3.
547 The change in voltage with inclusion of ICBA primarily
548 resulted in a suppression of the faster carrier lifetimes (Figure
549 3b), observed for the Br-containing perovskites, returning the
550 measured lifetimes to values comparable to those of the pure
551 MAPI/PCBM system. A small decrease in the charge density at
552 a given V_{OC} was also observed (Figure 3a), consistent with a
553 higher fullerene LUMO level, alongside an increase in device
554 ideality factor, consistent with a reduction in surface
555 recombination losses (Figure 4b). Although a full analysis of
556 the effects of ICBA substitution on device performance is
557 beyond the scope of this work, these results are also indicative
558 of the V_{OC} of bromine-substituted devices being increasingly
559 limited by higher surface recombination losses due to the larger
560 perovskite/fullerene LUMO level offset, with this effect being
561 most prominent at high light intensities.

4. DISCUSSION

562 We have reported above a combined differential charging and
563 photovoltage transient optoelectronic analysis of the open-
564 circuit voltage of planar organic/inorganic hybrid perovskite
565 solar cells as a function of light intensity and bromine
566 substitution. Using these data, a simple device model can
567 correctly predict (to within ± 5 mV) both the absolute device
568 open-circuit voltage and its dependence on light intensity and
569 bromine substitution without any fitting parameters. This
570 excellent agreement provides strong evidence for the validity of
571 both this simple model and this experimental approach for the
572 analysis of photovoltage generation in such devices. We first
573 discuss the general implications of this agreement, before going
574 on to discuss in detail the implications for the effect of bromine
575 substitution.

576 At low light levels, the measured charge density in the device
577 was found to be in good agreement with that estimated by
578 treating the device as a simple parallel-plate capacitor with
579 charge accumulating primarily on the device electrodes. At
580 higher light levels, the cell capacitance starts to increase

581 exponentially with applied potential, indicative of the increasing
582 dominance of an “electronic chemical capacitance”, correspond-
583 ing to increasing charge accumulation in the active layer(s) (or,
584 more specifically, the intrinsic or not strongly doped materials)
585 of the device, as illustrated in Figure 5a,c. This chemical
586 capacitance shifts with bromine substitution, consistent with at
587 least one photogenerated charge carrier accumulating in the
588 perovskite layer of the device at open-circuit and 1-sun
589 conditions. We note that, from the data herein, it is not
590 possible to rule out that one of the charge carriers contributing
591 to this chemical capacitance is accumulating in an interlayer
592 (i.e., holes on the PEDOT:PSS layer or electrons on the
593 PCBM). This contrasts with photoluminescence quenching
594 data, typically obtained at low light irradiances, which shows
595 strong photoluminescence quenching upon the addition of
596 either PEDOT:PSS or PCBM hole- and electron-collection
597 layers.¹³

598 The chemical capacitance of the devices studied here was
599 observed to increase exponentially with open-circuit voltage,
600 with an exponent of q/mkT , where $m = 3$ –5. This deviates
601 from the ideal behavior ($m = 2$) of an intrinsic semiconductor,
602 indicative of a significant tail of intraband gap or shallow trap
603 states, likely resulting from the presence of other (organic)
604 semiconducting layers. We note that this characteristic energy
605 for the tail of electronic states is larger than the observed
606 Urbach tail from optical measurements of perovskite films.^{53,54}
607 This distinction between optical and electronic measurements
608 of densities of states can also be observed in the difference we
609 observed between the increases in optical and effective
610 electronic band gaps with bromine substitution (see Table 1),
611 although a full understanding of this point, and the potential
612 impact of energetic alignment shifts at the device interfaces, is
613 beyond the scope of this study.

614 The charge-carrier lifetimes measured for the devices studied
615 herein were observed to be strongly dependent on light
616 intensity and charge-carrier density, as seen from an overall
617 order of recombination of $\delta > 3$. Lifetimes were in the range of
618 ~ 50 ns under 3-sun irradiation to 80 μs under 0.01-sun
619 irradiation (Figure 2a). The large retardation in lifetime with
620 decreased light irradiation can be attributed, in part, to a
621 proportionally increased charge localization on the device
622 electrodes compared to the active layer, resulting in a more
623 effective spatial separation of the photogenerated charges. At
624 higher light levels, the lifetime is likely to be dominated by the
625 recombination of charge carriers in the perovskite layer.
626 Although a full analysis of this light- and charge-density-
627 dependent behavior is beyond the scope of this work, the high-
628 light-level data, where the active-layer charge dominates,
629 indicates a charge-density-dependent bimolecular recombina-
630 tion rate coefficient (Figure S13) in the range from 1×10^{-10} to
631 $3 \times 10^{-10} \text{ cm}^3 \text{ s}^{-1}$ at light intensities in the range from 0.5 to 3
632 suns, reasonably consistent with previous observations from
633 transient optical and terahertz transient photoconductivity
634 measurements of MAPI layers alone.^{12,37}

635 Twenty percent bromine substitution was observed to result
636 in a 173 (± 7) mV increase in device V_{OC} relative to that of the
637 pure MAPI device. This increase in cell voltage was found to
638 result primarily from a 227 (± 9) mV increase in active-layer
639 effective electronic band gap as determined from the shift in
640 carrier density. This increase in perovskite electronic band gap
641 was partly offset by a 5-fold acceleration of recombination
642 kinetics (measured at matched charge densities), calculated to
643 result in a 56 (± 5) mV loss of cell voltage, resulting in a 643

644 calculated net voltage increase of 171 (± 10) mV, in excellent
645 agreement with experimental observations. In other words, the
646 acceleration of recombination losses with bromine substitution
647 prevented the device quasi-Fermi levels from approaching the
648 band edges as closely as would be obtained for the pure MAPI
649 device, as illustrated in Figure 5c,d. The shift in chemical
650 capacitance with bromine substitution confirms the assignment
651 of this chemical capacitance to one or both charge carriers
652 accumulating in the perovskite layer.

653 Regarding the origin of the acceleration of recombination
654 losses with bromine substitution, it appears consistent with that
655 reported previously for the formamidinium lead mixed-halide
656 system $\text{FAPb}(\text{Br}_x\text{I}_{1-x})_3$.³⁶ This was attributed to an increase in
657 disorder as a result of the disruption of material crystallinity⁹ or
658 a change in direct recombination as a result of varying band
659 edges. It might also result from changes in morphology possible
660 for the different Br compositions, although scanning electron
661 microscopy (SEM) images showed little change over the Br
662 range studied (Figure S14). If the perovskite/PCBM interface
663 is important, interpenetration of the PCBM into the perovskite
664 through grain boundaries might also influence the recombina-
665 tion.⁵⁵ A likely additional loss mechanism for full devices is
666 surface recombination, which is expected to increase as the
667 energetic offset between perovskite bands and both the PCBM
668 and PEDOT:PSS interlayers increases.³⁰ The increase in
669 $\text{CH}_3\text{NH}_3\text{Pb}(\text{I}_{1-x}\text{Br}_x)_3$ effective electronic band gap with
670 bromine substitution is accompanied by a decrease in the
671 ideality factor n_{id} , which could correlate with decreasing m value
672 in Figure 3a as δ remains constant.^{43,45,47} Studies of organic
673 solar cells have reported analogous changes in ideality in the
674 presence of a dominant surface recombination process.^{43,56} The
675 inclusion of 20% ICBA in the PCBM layer appears to reduce
676 the impact of recombination at the perovskite/PCBM interface,
677 showing an increase in n_{id} (and m), with the ability to harness
678 the potential voltage gain from the increase perovskite band
679 gap. Because of a higher-lying LUMO in ICBA, the energetic
680 position of the electron quasi-Fermi level generated in the
681 perovskite can be accommodated at a lower fullerene electron
682 population, resulting in reduced recombination at this interface.
683 These observations strongly suggest that optimization of
684 interlayers and electrodes might be required to achieve the
685 highest efficiencies possible from this particular architecture,
686 especially with mixed-halide perovskites.

5. CONCLUSIONS

687 In conclusion, the substitution of iodide with bromide in
688 $\text{CH}_3\text{NH}_3\text{Pb}(\text{I}_{1-x}\text{Br}_x)_3$ top-cathode planar hybrid perovskite
689 photovoltaics is shown to be an ideal system for demonstrating
690 the applicability of transient optoelectronic techniques for
691 probing the factors influencing the open-circuit voltage of these
692 devices. Differential charging measurements provide insight
693 into the internal energetics and relative charge accumulation,
694 whereas transient photovoltage measurements provide in-
695 formation on the kinetics of charge recombination. An increase
696 in V_{OC} for higher Br loadings is attributed to an increase in
697 energetics associated with the increase in perovskite band gap;
698 however, this is somewhat restricted by faster recombination,
699 likely due to increased surface recombination as a result of
700 poorer electrode/interlayer alignment with the perovskite
701 active layer. Remarkably, the measured lifetimes for these
702 devices are not dissimilar from those measured for common
703 organic bulk heterojunction devices. Although lifetimes in
704 OPVs benefit from charges residing on different molecules,

despite the energetic price in LUMO offset, perovskites appear
705 to have the ability to efficiently separate charge, giving long
706 carrier lifetimes compared to what might be expected from the
707 high mobility. Finally, the excellent correlation between
708 calculated and measured V_{OC} values demonstrates the
709 applicability of these optoelectronic techniques to the
710 description of device performance over a range of light
711 intensities relevant for standard operation. It is hoped the
712 transient optoelectronic methodology presented herein can be
713 used to further understand the origin of changes in
714 recombination in perovskite devices and light-induced band
715 gap pinning in future studies. 716

■ ASSOCIATED CONTENT

Supporting Information

The Supporting Information is available free of charge on the
ACS Publications website at DOI: 10.1021/acs.jpcc.7b02411. 720

Optical absorbance spectra of $\text{CH}_3\text{NH}_3\text{Pb}(\text{I}_{1-x}\text{Br}_x)_3$,
721 hysteresis effect on $J-V$ curves, $J-V$ parameter box
722 plots, linearity of J_{SC} with light intensity, charge
723 extraction/differential charging comparison, TPV rise
724 times, PCBM mobility calculations, $J-V$ curves as a
725 function of PCBM thickness, plot of Q vs V_{OC} , examples
726 of TPV and TPC transients, single-exponential TPV
727 fitting example, small-perturbation lifetime $\tau_{\Delta n}$ as a
728 function of V_{OC} , differential capacitance and Q as
729 functions of Br content, bimolecular recombination rate
730 constant as a function of active-layer charge-carrier
731 density, SEM images of $\text{CH}_3\text{NH}_3\text{Pb}(\text{I}_{1-x}\text{Br}_x)_3$ perovskite
732 films, calculation of total carrier lifetime, calculation of
733 kinetic voltage change, derivation of eq 4, and DC/TPV
734 model fitting parameters (PDF) 735

■ AUTHOR INFORMATION

Corresponding Author

*Phone: +44 0 20 7594 5321. E-mail: j.durrant@imperial.ac.uk. 738

ORCID

Scot Wheeler: 0000-0001-7335-5919 740

Thomas Kirchartz: 0000-0002-6954-8213 741

James R. Durrant: 0000-0001-8353-7345 742

Notes

The authors declare no competing financial interest. 744

■ ACKNOWLEDGMENTS

We acknowledge funding from the Engineering and Physical
746 Sciences Research Council (EPSRC) Projects No. EP/J500021
747 and EP/I019278, the Supergen programme (EP/J017361/1
748 and EP/M014797/1) and the Doctoral Training Centre in
749 Science and Application of Plastic Electronic Materials (EP/
750 G037515), as well as the Welsh Assembly Government Sêr
751 Cymru Solar Project. 752

■ REFERENCES

- 753 (1) Saliba, M.; Matsui, T.; Seo, J.-Y.; Domanski, K.; Correa-Baena, J.-
754 P.; Nazeeruddin, M. K.; Zakeeruddin, S. M.; Tress, W.; Abate, A.;
755 Hagfeldt, A.; et al. Cesium-Containing Triple Cation Perovskite Solar
756 Cells: Improved Stability, Reproducibility and High Efficiency. *Energy*
757 *Environ. Sci.* **2016**, *9*, 1989–1997. 758
- (2) Saliba, M.; Orlandi, S.; Matsui, T.; Aghazada, S.; Cavazzini, M.;
759 Correa-Baena, J.-P.; Gao, P.; Scopelliti, R.; Mosconi, E.; Dahmen, K.-
760 H.; et al. A Molecularly Engineered Hole-Transporting Material for
761 Efficient Perovskite Solar Cells. *Nature Energy* **2016**, *1*, 15017. 762

- (3) Bi, D.; Tress, W.; Dar, M. I.; Gao, P.; Luo, J.; Renevier, C.; Schenk, K.; Abate, A.; Giordano, F.; Correa Baena, J.-P. Efficient Luminescent Solar Cells Based on Tailored Mixed-Cation Perovskites. *Sci. Adv.* **2016**, *2*, e1501170.
- (4) Jeon, N. J.; Noh, J. H.; Yang, W. S.; Kim, Y. C.; Ryu, S.; Seo, J.; Seok, S. I. Compositional Engineering of Perovskite Materials for High-Performance Solar Cells. *Nature* **2015**, *517*, 476–480.
- (5) Wu, C.-G.; Chiang, C.-H.; Chang, S. H. A Perovskite Cell with a Record-High- V_{oc} of 1.61 V Based on Solvent Annealed $\text{CH}_3\text{NH}_3\text{PbBr}_3/\text{ICBA}$ Active Layer. *Nanoscale* **2016**, *8*, 4077–4085.
- (6) Ryu, S.; Noh, J. H.; Jeon, N. J.; Chan Kim, Y.; Yang, W. S.; Seo, J.; Seok, S. I. Voltage Output of Efficient Perovskite Solar Cells with High Open-Circuit Voltage and Fill Factor. *Energy Environ. Sci.* **2014**, *7*, 2614–2618.
- (7) Edri, E.; Kirmayer, S.; Cahen, D.; Hodes, G. High Open-Circuit Voltage Solar Cells Based on Organic–Inorganic Lead Bromide Perovskite. *J. Phys. Chem. Lett.* **2013**, *4*, 897–902.
- (8) Eperon, G. E.; Stranks, S. D.; Menelaou, C.; Johnston, M. B.; Herz, L. M.; Snaith, H. J. Formamidinium Lead Trihalide: A Broadly Tunable Perovskite for Efficient Planar Heterojunction Solar Cells. *Energy Environ. Sci.* **2014**, *7*, 982–988.
- (9) Noh, J. H.; Im, S. H.; Heo, J. H.; Mandal, T. N.; Seok, S. I. Chemical Management for Colorful, Efficient, and Stable Inorganic–Organic Hybrid Nanostructured Solar Cells. *Nano Lett.* **2013**, *13*, 1764–1769.
- (10) Correa Baena, J. P.; Steier, L.; Tress, W.; Saliba, M.; Neutzner, S.; Matsui, T.; Giordano, F.; Jacobsson, T. J.; Srimath Kandada, A. R.; Zakeeruddin, S. M.; et al. Highly Efficient Planar Perovskite Solar Cells through Band Alignment Engineering. *Energy Environ. Sci.* **2015**, *8*, 2928–2934.
- (11) Wehrenfennig, C.; Eperon, G. E.; Johnston, M. B.; Snaith, H. J.; Herz, L. M. High Charge Carrier Mobilities and Lifetimes in Organolead Trihalide Perovskites. *Adv. Mater.* **2014**, *26*, 1584–1589.
- (12) Wehrenfennig, C.; Liu, M.; Snaith, H. J.; Johnston, M. B.; Herz, L. M. Charge-Carrier Dynamics in Vapour-Deposited Films of the Organolead Halide Perovskite $\text{CH}_3\text{NH}_3\text{Pb}_{1-x}\text{Cl}_x$. *Energy Environ. Sci.* **2014**, *7*, 2269–2275.
- (13) Stranks, S. D.; Eperon, G. E.; Grancini, G.; Menelaou, C.; Alcocer, M. J. P.; Leijtens, T.; Herz, L. M.; Petrozza, A.; Snaith, H. J. Electron-Hole Diffusion Lengths Exceeding 1 Micrometer in an Organometal Trihalide Perovskite Absorber. *Science* **2013**, *342*, 341–344.
- (14) Shi, D.; Adinolfi, V.; Comin, R.; Yuan, M.; Alarousu, E.; Buin, A.; Chen, Y.; Hoogland, S.; Rothenberger, A.; Katsiev, K.; et al. Low Trap-State Density and Long Carrier Diffusion in Organolead Trihalide Perovskite Single Crystals. *Science* **2015**, *347*, 519–522.
- (15) Credgington, D.; Liu, S.-W.; Nelson, J.; Durrant, J. R. In Situ Measurement of Energy Level Shifts and Recombination Rates in Subphthalocyanine/C60 Bilayer Solar Cells. *J. Phys. Chem. C* **2014**, *118*, 22858–22864.
- (16) Barnes, P. R. F.; Miettunen, K.; Li, X.; Anderson, A. Y.; Bessho, T.; Gratzel, M.; O'Regan, B. C. Interpretation of Photoelectronic Transient and Charge Extraction Measurements in Dye-Sensitized Solar Cells. *Adv. Mater.* **2013**, *25*, 1881–1922.
- (17) Foertig, A.; Rauh, J.; Dyakonov, V.; Deibel, C. Shockley Equation Parameters of P3HT:PCBM Solar Cells Determined by Transient Techniques. *Phys. Rev. B: Condens. Matter Mater. Phys.* **2012**, *86*, 115302.
- (18) O'Regan, B. C.; Barnes, P. R. F.; Li, X.; Law, C.; Palomares, E.; Marin-Belouqui, J. M. Photoelectronic Studies of Methylammonium Lead Iodide Perovskite Solar Cells with Mesoporous TiO_2 : Separation of Electronic and Chemical Charge Storage, Understanding Two Recombination Lifetimes, and the Evolution of Band Offsets During J–V Hysteresis. *J. Am. Chem. Soc.* **2015**, *137*, 5087–5099.
- (19) Shao, Y.; Yuan, Y.; Huang, J. Correlation of Energy Disorder and Open-Circuit Voltage in Hybrid Perovskite Solar Cells. *Nature Energy* **2016**, *1*, 15001.
- (20) Marin-Belouqui, J. M.; Lanzetta, L.; Palomares, E. Decreasing Charge Losses in Perovskite Solar Cells through mp-TiO₂/MAPI Interface Engineering. *Chem. Mater.* **2016**, *28*, 207–213.
- (21) Marin-Belouqui, J. M.; Hernandez, J. P.; Palomares, E. Photo-Induced Charge Recombination Kinetics in $\text{MAPbI}_{3-x}\text{Cl}_x$ Perovskite-Like Solar Cells Using Low Band-Gap Polymers as Hole Conductors. *Chem. Commun.* **2014**, *50*, 14566–14569.
- (22) Carnie, M. J.; Troughton, J.; Regan, B. O.; Barnes, P.; Bryant, D.; Watson, T.; Worsley, D. Identifying Recombination Mechanisms through Materials Development in Perovskite Solar Cells. Presented at the 2015 IEEE 42nd Photovoltaic Specialist Conference (PVSC), New Orleans, LA, Jun 14–19, 2015.
- (23) Calado, P.; Telford, A. M.; Bryant, D.; Li, X.; Nelson, J.; O'Regan, B. C.; Barnes, P. R. Evidence for Ion Migration in Hybrid Perovskite Solar Cells with Minimal Hysteresis. *Nat. Commun.* **2016**, *7*, 13831.
- (24) Bryant, D.; Wheeler, S.; O'Regan, B. C.; Watson, T.; Barnes, P. R. F.; Worsley, D.; Durrant, J. Observable Hysteresis at Low Temperature in “Hysteresis Free” Organic–Inorganic Lead Halide Perovskite Solar Cells. *J. Phys. Chem. Lett.* **2015**, *6*, 3190–3194.
- (25) van Reenen, S.; Kemerink, M.; Snaith, H. J. Modeling Anomalous Hysteresis in Perovskite Solar Cells. *J. Phys. Chem. Lett.* **2015**, *6*, 3808–3814.
- (26) Rajagopal, A.; Williams, S. T.; Chueh, C.-C.; Jen, A. K. Y. Abnormal Current–Voltage Hysteresis Induced by Reverse Bias in Organic–Inorganic Hybrid Perovskite Photovoltaics. *J. Phys. Chem. Lett.* **2016**, *7*, 995–1003.
- (27) McMeekin, D. P.; Sadoughi, G.; Rehman, W.; Eperon, G. E.; Saliba, M.; Hörlantner, M. T.; Haghighirad, A.; Sakai, N.; Korte, L.; Rech, B.; et al. A Mixed-Cation Lead Mixed-Halide Perovskite Absorber for Tandem Solar Cells. *Science* **2016**, *351*, 151–155.
- (28) Suarez, B.; Gonzalez-Pedro, V.; Ripolles, T. S.; Sanchez, R. S.; Otero, L.; Mora-Sero, I. Recombination Study of Combined Halides (Cl, Br, I) Perovskite Solar Cells. *J. Phys. Chem. Lett.* **2014**, *5*, 1628–1635.
- (29) Sadhanala, A.; Deschler, F.; Thomas, T. H.; Dutton, S. E.; Goedel, K. C.; Hanusch, F. C.; Lai, M. L.; Steiner, U.; Bein, T.; Docampo, P.; et al. Preparation of Single-Phase Films of $\text{CH}_3\text{NH}_3\text{Pb}(I_{1-x}\text{Br}_x)_3$ with Sharp Optical Band Edges. *J. Phys. Chem. Lett.* **2014**, *5*, 2501–2505.
- (30) Schulz, P.; Edri, E.; Kirmayer, S.; Hodes, G.; Cahen, D.; Kahn, A. Interface Energetics in Organo-Metal Halide Perovskite-Based Photovoltaic Cells. *Energy Environ. Sci.* **2014**, *7*, 1377–1381.
- (31) Seo, J.; Park, S.; Chan Kim, Y.; Jeon, N. J.; Noh, J. H.; Yoon, S. C.; Seok, S. I. Benefits of Very Thin PCBM and LiF Layers for Solution-Processed p–i–n Perovskite Solar Cells. *Energy Environ. Sci.* **2014**, *7*, 2642–2646.
- (32) Credgington, D.; Durrant, J. R. Insights from Transient Photoelectronic Analyses on the Open-Circuit Voltage of Organic Solar Cells. *J. Phys. Chem. Lett.* **2012**, *3*, 1465–1478.
- (33) Hoke, E. T.; Slotcavage, D. J.; Dohner, E. R.; Bowring, A. R.; Karunadasa, H. I.; McGehee, M. D. Reversible Photo-Induced Trap Formation in Mixed-Halide Hybrid Perovskites for Photovoltaics. *Chemical Science* **2015**, *6*, 613–617.
- (34) Cai, B.; Xing, Y.; Yang, Z.; Zhang, W.-H.; Qiu, J. High Performance Hybrid Solar Cells Sensitized by Organolead Halide Perovskites. *Energy Environ. Sci.* **2013**, *6*, 1480–1485.
- (35) Yoon, S. J.; Draguta, S.; Manser, J. S.; Sharia, O.; Schneider, W. F.; Kuno, M.; Kamat, P. V. Tracking Iodide and Bromide Ion Segregation in Mixed Halide Lead Perovskites During Photo-irradiation. *ACS Energy Letters* **2016**, *1*, 290–296.
- (36) Rehman, W.; Milot, R. L.; Eperon, G. E.; Wehrenfennig, C.; Boland, J. L.; Snaith, H. J.; Johnston, M. B.; Herz, L. M. Charge-Carrier Dynamics and Mobilities in Formamidinium Lead Mixed-Halide Perovskites. *Adv. Mater.* **2015**, *27*, 7938–7944.
- (37) Manser, J. S.; Kamat, P. V. Band Filling with Free Charge Carriers in Organometal Halide Perovskites. *Nat. Photonics* **2014**, *8*, 737–743.

- 898 (38) Frost, J. M.; Butler, K. T.; Walsh, A. Molecular Ferroelectric
899 Contributions to Anomalous Hysteresis in Hybrid Perovskite Solar
900 Cells. *APL Mater.* **2014**, *2*, 081506.
- 901 (39) Onoda-Yamamuro, N.; Matsuo, T.; Suga, H. Dielectric Study of
902 $\text{CH}_3\text{NH}_3\text{PbX}_3$ ($X = \text{Cl}, \text{Br}, \text{I}$). *J. Phys. Chem. Solids* **1992**, *53*, 935–939.
- 903 (40) O'Regan, B. C.; Bakker, K.; Kroeze, J.; Smit, H.; Sommeling, P.;
904 Durrant, J. R. Measuring Charge Transport from Transient Photo-
905 voltage Rise Times. A New Tool to Investigate Electron Transport in
906 Nanoparticle Films. *J. Phys. Chem. B* **2006**, *110*, 17155–17160.
- 907 (41) Garcia-Belmonte, G.; Munar, A.; Barea, E. M.; Bisquert, J.;
908 Ugarte, I.; Pacios, R. Charge Carrier Mobility and Lifetime of Organic
909 Bulk Heterojunctions Analyzed by Impedance Spectroscopy. *Org.*
910 *Electron.* **2008**, *9*, 847–851.
- 911 (42) Foster, S.; Deledalle, F.; Mitani, A.; Kimura, T.; Kim, K.-B.;
912 Okachi, T.; Kirchartz, T.; Oguma, J.; Miyake, K.; Durrant, J. R.
913 Electron Collection as a Limit to Polymer:PCBM Solar Cell Efficiency:
914 Effect of Blend Microstructure on Carrier Mobility and Device
915 Performance in PTB7:PCBM. *Adv. Energy Mater.* **2014**, *4*, 1400311.
- 916 (43) Wheeler, S.; Deledalle, F.; Tokmoldin, N.; Kirchartz, T.; Nelson,
917 J.; Durrant, J. R. Influence of Surface Recombination on Charge-
918 Carrier Kinetics in Organic Bulk Heterojunction Solar Cells with
919 Nickel Oxide Interlayers. *Phys. Rev. Appl.* **2015**, *4*, 024020.
- 920 (44) Foertig, A.; Kniepert, J.; Gluecker, M.; Brenner, T.; Dyakonov,
921 V.; Neher, D.; Deibel, C. Nongeminate and Geminate Recombination
922 in PTB7:PCBM Solar Cells. *Adv. Funct. Mater.* **2014**, *24*, 1306–1311.
- 923 (45) Kirchartz, T.; Nelson, J. Meaning of Reaction Orders in
924 Polymer:Fullerene Solar Cells. *Phys. Rev. B: Condens. Matter Mater.*
925 *Phys.* **2012**, *86*, 165201.
- 926 (46) Deledalle, F.; Shakya Tuladhar, P.; Nelson, J.; Durrant, J. R.;
927 Kirchartz, T. Understanding the Apparent Charge Density Depend-
928 ence of Mobility and Lifetime in Organic Bulk Heterojunction Solar
929 Cells. *J. Phys. Chem. C* **2014**, *118*, 8837–8842.
- 930 (47) Kirchartz, T.; Deledalle, F.; Tuladhar, P. S.; Durrant, J. R.;
931 Nelson, J. On the Differences between Dark and Light Ideality Factor
932 in Polymer:Fullerene Solar Cells. *J. Phys. Chem. Lett.* **2013**, *4*, 2371–
933 2376.
- 934 (48) Kirchartz, T.; Pieters, B. E.; Kirkpatrick, J.; Rau, U.; Nelson, J.
935 Recombination Via Tail States in Polythiophene:Fullerene Solar Cells.
936 *Phys. Rev. B: Condens. Matter Mater. Phys.* **2011**, *83*, 115209.
- 937 (49) Marinova, N.; Tress, W.; Humphry-Baker, R.; Dar, M. I.;
938 Bojinov, V.; Zakeeruddin, S. M.; Nazeeruddin, M. K.; Grätzel, M. Light
939 Harvesting and Charge Recombination in $\text{CH}_3\text{NH}_3\text{PbI}_3$ Perovskite
940 Solar Cells Studied by Hole Transport Layer Thickness Variation. *ACS*
941 *Nano* **2015**, *9*, 4200–4209.
- 942 (50) Pockett, A.; Eperon, G. E.; Peltola, T.; Snaith, H. J.; Walker, A.;
943 Peter, L. M.; Cameron, P. J. Characterization of Planar Lead Halide
944 Perovskite Solar Cells by Impedance Spectroscopy, Open-Circuit
945 Photovoltage Decay, and Intensity-Modulated Photovoltage/Photo-
946 current Spectroscopy. *J. Phys. Chem. C* **2015**, *119*, 3456–3465.
- 947 (51) Yao, J.; Kirchartz, T.; Vezie, M. S.; Faist, M. A.; Gong, W.; He,
948 Z.; Wu, H.; Troughton, J.; Watson, T.; Bryant, D.; Nelson, J.
949 Quantifying Losses in Open-Circuit Voltage in Solution-Processable
950 Solar Cells. *Phys. Rev. Appl.* **2015**, *4*, 014020.
- 951 (52) Tress, W.; Marinova, N.; Inganäs, O.; Nazeeruddin, M. K.;
952 Zakeeruddin, S. M.; Graetzel, M. Predicting the Open-Circuit Voltage
953 of $\text{CH}_3\text{NH}_3\text{PbI}_3$ Perovskite Solar Cells Using Electroluminescence and
954 Photovoltaic Quantum Efficiency Spectra: The Role of Radiative and
955 Non-Radiative Recombination. *Adv. Energy Mater.* **2015**, *5*, 1400812.
- 956 (53) De Wolf, S.; Holovsky, J.; Moon, S.-J.; Löper, P.; Niesen, B.;
957 Ledinsky, M.; Haug, F.-J.; Yum, J.-H.; Ballif, C. Organometallic Halide
958 Perovskites: Sharp Optical Absorption Edge and Its Relation to
959 Photovoltaic Performance. *J. Phys. Chem. Lett.* **2014**, *5*, 1035–1039.
- 960 (54) Leguy, A. M. A.; Azarhoosh, P.; Alonso, M. I.; Campoy-Quiles,
961 M.; Weber, O. J.; Yao, J.; Bryant, D.; Weller, M. T.; Nelson, J.; Walsh,
962 A.; et al. Experimental and Theoretical Optical Properties of
963 Methylammonium Lead Halide Perovskites. *Nanoscale* **2016**, *8*,
964 6317–6327.
- 965 (55) Paulke, A.; Stranks, S. D.; Kniepert, J.; Kurpiers, J.; Wolff, C. M.;
966 Schön, N.; Snaith, H. J.; Brenner, T. J. K.; Neher, D. Charge Carrier
Recombination Dynamics in Perovskite and Polymer Solar Cells. *Appl.*
Phys. Lett. **2016**, *108*, 113505.
- (56) Schäfer, S.; Petersen, A.; Wagner, T. A.; Kniprath, R.;
Lingenfeller, D.; Zen, A.; Kirchartz, T.; Zimmermann, B.; Würfel,
U.; Feng, X.; Mayer, T. Influence of the Indium Tin Oxide/Organic
Interface on Open-Circuit Voltage, Recombination, and Cell
Degradation in Organic Small-Molecule Solar Cells. *Phys. Rev. B:*
Condens. Matter Mater. Phys. **2011**, *83*, 165311.